Drewitt, J., Walter, M., Zhang, H., McMahon, S. C., Edwards, D., Heinen, B., Lord, O., Anzellini, S., & Kleppe, A. (2019). The fate of carbonate in oceanic crust subducted into earth's lower mantle. *Earth and Planetary Science Letters*, *511*, 213-222. https://doi.org/10.1016/j.epsl.2019.01.041

Earth and Planetary Science Letters 511 (2019) 213–222

Contents lists available at ScienceDirect

Earth and Planetary Science Letters

www.elsevier.com/locate/epsl

The fate of carbonate in oceanic crust subducted into earth's lower mantle

James W.E. Drewitt [a], Michael J. Walter [a,b,*], Hongluo Zhang [a,c], Sorcha C. McMahon [a], David Edwards [a], Benedict J. Heinen [a], Oliver T. Lord [a], Simone Anzellini [d], Annette K. Kleppe [d]

[a] School of Earth Sciences, University of Bristol, Wills Memorial Building, Queens Road, BS8 1RJ, United Kingdom
[b] Geophysical Laboratory, Carnegie Institution for Science, 5251 Broad Branch Road NW, Washington, DC 20015, USA
[c] School of Earth and Space Sciences, University of Science and Technology of China, 96 Jinzhai RD, Hefei, Anhui 230026, PR China
[d] Diamond Light Source Ltd, Diamond House, Harwell Science and Innovation Campus, Chilton, OX11 0DE, United Kingdom

ARTICLE INFO

Article history:
Received 6 August 2018
Received in revised form 21 January 2019
Accepted 24 January 2019
Available online xxxx
Editor: M. Bickle

Keywords:
carbonate
subduction
lower mantle
decarbonation
diamond

ABSTRACT

We report on laser-heated diamond anvil cell (LHDAC) experiments in the FeO–MgO–SiO_2–CO_2 (FMSC) and CaO–MgO–SiO_2–CO_2 (CMSC) systems at lower mantle pressures designed to test for decarbonation and diamond forming reactions. Sub-solidus phase relations based on synthesis experiments are reported in the pressure range of ~35 to 90 GPa at temperatures of ~1600 to 2200 K. Ternary bulk compositions comprised of mixtures of carbonate and silica are constructed such that decarbonation reactions produce non-ternary phases (e.g. bridgmanite, Ca-perovskite, diamond, CO_2–V), and synchrotron X-ray diffraction and micro-Raman spectroscopy are used to identify the appearance of reaction products. We find that carbonate phases in these two systems react with silica to form bridgmanite ±Ca-perovskite + CO_2 at pressures in the range of ~40 to 70 GPa and 1600 to 1900 K in decarbonation reactions with negative Clapeyron slopes. Our results show that decarbonation reactions form an impenetrable barrier to subduction of carbonate in oceanic crust to depths in the mantle greater than ~1500 km. We also identify carbonate and CO_2–V dissociation reactions that form diamond plus oxygen. On the basis of the observed decarbonation reactions we predict that the ultimate fate of carbonate in oceanic crust subducted into the deep lower mantle is in the form of refractory diamond in the deepest lower mantle along a slab geotherm and throughout the lower mantle along a mantle geotherm. Diamond produced in oceanic crust by subsolidus decarbonation is refractory and immobile and can be stored at the base of the mantle over long timescales, potentially returning to the surface in OIB magmas associated with deep mantle plumes.

1. Introduction

Carbon is essential for habitability at earth's surface and understanding how it cycles through exterior and interior reservoirs is fundamental for modelling the evolution of carbon through geological time (Sleep and Zahnle, 2001). The abundance of carbon in earth's interior is highly uncertain with estimates for carbon in bulk silicate earth varying by more than an order of magnitude from ~20 to 800 ppm (Dasgupta and Hirschmann, 2010; Marty, 2012; Sleep and Zahnle, 2001), and estimates for the core ranging from very little to several weight% (Chen et al., 2014; Dasgupta and Walker, 2008; Wood et al., 2013).

While absolute carbon abundances are challenging to constrain, estimates of the H/C ratio in bulk silicate earth indicate that this ratio is greater than the primitive chondritic ratio (Halliday, 2013; Hirschmann and Dasgupta, 2009; Marty, 2012), a feature which can ostensibly be explained by solution of carbon into iron-rich liquid metal during high pressure–temperature core segregation. However, H/C in earth's exosphere (crust and atmosphere) is also markedly higher than in the upper mantle source of basalts, a feature that requires fractionation between the exosphere and the mantle reservoir independent of core formation, suggesting a long-lived deep mantle reservoir, possibly in the lower mantle (Hirschmann and Dasgupta, 2009). Carbon sequestration in the mantle may have occurred early during earth's accretion and magma ocean stage, or by continuous subduction of carbon-bearing oceanic crustal materials into the deep mantle throughout much of earth's history.

* Corresponding author.
E-mail address: mwalter@carnegiescience.edu (M.J. Walter).

https://doi.org/10.1016/j.epsl.2019.01.041

Carbon is added to the top few hundred meters of oceanic crust largely as carbonate by reaction with seawater, and average basaltic oceanic crust is estimated to contain about 2.5 wt.% CO_2 (Coogan and Dosso, 2015; Coogan and Gillis, 2013). Carbon is also deposited as either carbonate or other reduced carbon compounds in subducted sediments (Plank and Langmuir, 1998). Estimates of the global return flux of carbon to the mantle (i.e. past the volcanic front) by subduction of oceanic lithosphere are inexact, ranging from negligible to considerable (e.g., ~60 Mton/year) (Dasgupta and Hirschmann, 2010; Kelemen and Manning, 2015).

1.1. Carbonate in the deep mantle

The form of carbon in earth's deep interior depends on many factors including pressure, temperature and bulk composition. In peridotitic mantle compositions carbonate may not be stable at depths below a few hundred kilometers due to the low intrinsic oxygen activity of peridotitic mineral assemblages, and the stable form of carbon will be diamond or iron carbide (Frost and McCammon, 2008; Stagno et al., 2013). Carbonate stability in subducted basaltic oceanic crust depends especially on oxygen activity and carbonate solubility in aqueous fluids released from the slab during dehydration, which depend on the pressure–temperature path during subduction and the metamorphic mineral assemblage. However, modelling of oceanic crustal oxygen activity and slab devolatilization processes using phase equilibrium data indicate that more than half of subducted carbonate may be transported past the volcanic front and into the deeper mantle (Gorman et al., 2006; Kerrick and Connolly, 2001; Molina and Poli, 2000; Poli et al., 2009; Stagno et al., 2015; Yaxley and Green, 1994). Indeed, the presence of carbonate minerals included in sublithospheric diamonds provide material evidence for carbonate subducted at least to transition zone depths (Brenker et al., 2007; Bulanova et al., 2010).

In basaltic oceanic crustal compositions carbonate minerals coexist with majoritic garnet and stishovite in the transition zone (Sekine et al., 1986), and with bridgmanite, Ca-perovskite, an SiO_2 polymorph (stishovite, $CaCl_2$-type phase or seifertite) and an aluminous phase (either the NAL or CF-type phase) in the lower mantle (Ono et al., 2001; Ricolleau et al., 2010). In the $CaCO_3$–$MgCO_3$ system dolomite breaks down to magnesite + aragonite at pressures between ~6 and 10 GPa and 1200 to 1500 K (Luth, 2001), and which of these phases dominates in basaltic protoliths depends critically on bulk composition. In Mg-rich protoliths magnesite is the dominant carbonate coexisting with a Na-carbonate phase in the deep upper mantle and transition zone (Thomson et al., 2016b), whereas in more calcic bulk compositions aragonite may become the dominant carbonate phase (Kiseeva et al., 2013). At lower mantle pressures the stable carbonate phase or phases in a basaltic protolith is uncertain. In the endmember $CaCO_3$ system aragonite is stable at pressures >~5 GPa and is replaced by $CaCO_3$–VII at ~25 GPa, by post-aragonite at ~40 GPa and a pyroxene-structured $CaCO_3$–P2 phase at pressure of ~80 GPa or more (Bayarjargal et al., 2018; Gavryushkin et al., 2017; Lobanov et al., 2017; Ono et al., 2007; Zhang et al., 2018). No experimental data exist in the system magnesite-dolomite at the investigated experimental conditions, however, on the basis of the closure of the magnesite-dolomite solvus in the phase diagram at 6 GPa (Buob et al., 2006), it seems probable that at lower mantle temperatures the system is super-solvus. In the endmember $MgCO_3$ system magnesite is reported to be stable up to deep lower mantle pressures where it transforms to the magnesite-II phase somewhere in the range of 80 to 115 GPa (Biellmann et al., 1993; Isshiki et al., 2004; Maeda et al., 2017; Oganov et al., 2008). In the more complex Fe–Mg–Ca carbonate system dolomite has an enhanced stability and is replaced with dolomite II above ~17 GPa, dolomite III above ~35 GPa and dolomite IV in the deep lower mantle (Mao et al., 2011; Merlini et al., 2017; Merlini et al., 2012). Thus, a dolomite phases could be an important carbonate in subducted lithologies in the lower mantle.

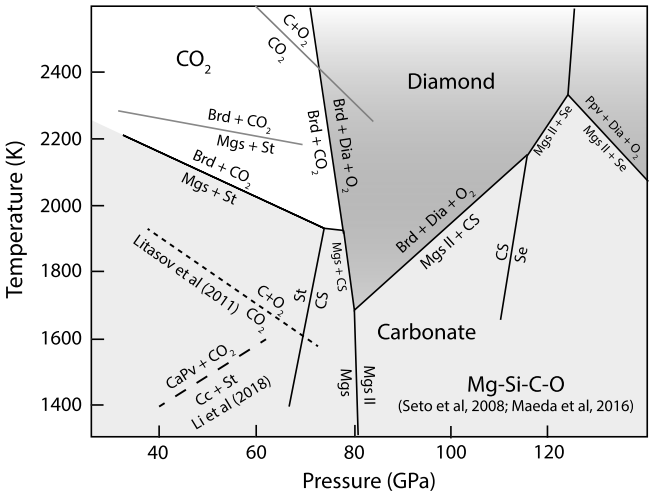

Fig. 1. Pressure–temperature diagram showing phase relations in the MgO–SiO_2–CO_2 (MSC) system at lower mantle pressures. The black solid reaction boundaries are from Maeda et al. (2017) and the grey boundaries are from Seto et al. (2008). The short-dashed line is the CO_2 breakdown reaction in the C–O system as determined by Litasov et al. (2011). The long-dashed line is the decarbonation reaction in the CaO-SiO_2–CO_2 (CSC) system as determined by Li et al. (2018). Brd = bridgmanite; Mgs = magnesite; MgsII = magnesite II; Cc = calcite; CaPv = Ca-perovskite; St = stishovite; CS = $CaCl_2$-structured SiO_2; Se = seifertite; Ppv = post-perovskite; Dia = diamond.

Decarbonation of carbonate in the presence of a free silica phase has been reported experimentally and predicted theoretically at lower mantle pressures and high temperatures in the systems MgO–SiO_2–CO_2 (MSC) and CaO–SiO_2–CO_2 (CSC) (Li et al., 2018; Maeda et al., 2017; Oganov et al., 2008; Seto et al., 2008; Takafuji et al., 2006; Zhang et al., 2018) via reactions of the form:

$$MgCO_3 + SiO_2 \rightarrow MgSiO_3 + CO_2, \quad (1)$$

$$CaCO_3 + SiO_2 \rightarrow CaSiO_3 + CO_2, \quad (2)$$

$$MgCO_3 + SiO_2 \rightarrow MgSiO_3 + C + O_2. \quad (3)$$

Fig. 1 shows phase relations summarising the results of recent studies in the MSC and CSC systems. Maeda et al. (2017) and Seto et al. (2008) reported that decarbonation reaction (1) occurs at ~1900 to 2200 K at pressures of 40 to 80 GPa with a negative Clapyron slope, and suggested that carbonate may be stable along a cold subducted slab geotherm. Maeda et al. reported a CO_2 breakdown reaction resulting in a diamond stability region extending to a minimum temperature of ~1700 K at 80 GPa that is caused by the intersection of the decarbonation reaction with the phase transition from magnesite to magnesite II, and they postulated a region where diamond would form in the mid-lower mantle in subducted oceanic crust on this basis. In the CSC system, Li et al. (2018) reported on experiments showing that $CaCO_3$ decarbonation in the presence of silica occurs at ~1400–1600 K at 40 to 60 GPa but with a positive Clapyron slope. Zhang et al. extended these findings and predict from theory that $CaCO_3$ decarbonates in the presence of silica at temperatures of ~1400 to 2000 K from 40 to 140 GPa, and also suggest a low-temperature excursion of the reaction in the mid-lower mantle due to a phase change from post-aragonite to $CaCO_3$–P2 phase.

The experiments presented in this study are explicitly designed to investigate the fate of the carbonate component in basalt

Table 1
Starting compositions (wt%).

	CMSC_3	FMSC_1
$MgCO_3$	42.66	44.86
$FeCO_3$	–	15.38
$CaCO_3$	16.89	–
SiO_2	40.45	39.76

that is subducted into the lower mantle, and to determine what form that carbon would take in oceanic crust subducted to the base of the mantle where it can be plausibly stored on geologically long timescales. We test for high-pressure decarbonation and diamond forming reactions in the systems $CaO–MgO–SiO_2–CO_2$ (CMSC) and $FeO–MgO–SiO_2–CO_2$ (FMSC) at lower mantle pressures, representing an increase in chemical complexity approaching natural compositions. We report on LHDAC experiments and subsequent analysis of the recovered run products by synchrotron X-ray diffraction and micro-Raman spectroscopy, and use these data to constrain the stability of carbonate in deeply subducted oceanic crust.

2. Material and methods

2.1. Starting compositions

Starting compositions were synthesized in the CMSC and FMSC systems by mixing carbonates with silica glass (Table 1). Fig. 2 shows chemographic relations in these systems that illustrate the method used here to deduce decarbonation reactions. The starting compositions are designed to lie on a ternary plane described by carbonate (magnesite + calcite or magnesite + siderite) and SiO_2. If carbonate remains stable in the presence of SiO_2, then the system will remain ternary, and at high pressure and temperature the expectation would be for a carbonate solid solution (or possibly two carbonate phases) to coexist with an SiO_2 polymorph. However, if a decarbonation reaction occurs, then the system will become quaternary (or quinary if the products are $C + O_2$) via reactions such as:

$$(Mg, Fe)CO_3 + SiO_2 = (Mg, Fe)SiO_3 + CO_2 \quad (4)$$

$$CaMg(CO_3)_2 + 2SiO_2 = MgSiO_3 + CaSiO_3 + 2CO_2 \quad (5)$$

The key advantage to making compositions on the ternary plane is that recognition of a decarbonation reaction only requires identification of the presence of non-ternary phases in quenched run products (e.g. bridgmanite (brd), Ca-perovskite (CaPv), diamond or CO_2). Another advantage is that potential variations in the starting compositions loaded into the DAC due to the inherently small sample size are irrelevant, because any starting mixture is confined to lie on the carbonate plus silica plane.

In the CMSC system (Fig. 2a) the starting composition is a mixture comprising magnesite (natural crystal with $< 0.5\%$ minor and trace elements) and calcite (Alfa Aesar 99.9%) in a 3:1 ratio plus SiO_2 glass (Corning 99.99%). In the FMSC system (Fig. 2b) we made a composition with a 4:1 molar mixture of magnesite and siderite (synthesized as described in Thomson et al. 2016a, 2016b) plus SiO_2 glass. In both mixtures we purposefully designed the compositions so that carbonate would be the limiting reactant and all experiments contain excess SiO_2 (see Fig. 2).

Approximately 10 wt.% Pt-black was added as a laser coupler to the Fe-free CMSC composition. All mixtures were ground under acetone in an agate mortar for ∼2 to 4 hours to achieve homogeneous, finely powered samples with the grain size mode in the range of ∼1 to 3 μm. We note that any contamination of the starting mixture with SiO_2 from the agate mortar will have no effect on the phase relations as the bulk composition remains on the ternary plane. Following grinding, the powdered samples were stored at 120 °C in a vacuum oven to minimize absorption of atmospheric water.

2.2. Laser-heated diamond anvil cell experiments

High pressure (P) and temperature (T) experiments were performed in Princeton-type symmetric diamond anvil cells with double-sided laser heating. Diamonds with culet diameters ranging from 200 to 250 μm were employed. Sample chambers ∼50 to 70 μm in diameter were laser-drilled into Re gaskets preindented to a thickness of ∼50 μm. Powdered starting materials were pressed between two opposing diamonds with culet diameters of 500 μm to produce thin foils ∼10 to 15 μm thick. A ∼30 to 50 μm diameter chip of this material was loaded into each sample chamber between ∼15 to 20 μm thick laser-cut form-fitting discs of NaCl to thermally insulate the samples from the diamonds.

High temperature conditions were achieved using the Bristol laser-heating system described in detail by Lord et al. (2014a, 2014b), with double-sided heating from two 100 W Yb-doped yttrium-aluminium-garnet (YAG) fibre lasers. Beam shaping optics are used to provide a 'flat top' beam profile over an ∼20 μm spot to reduce radial temperature gradients. Temperature was measured using standardized radiometric techniques as described in detail previously (Lord et al., 2014a; Walter and Koga, 2004; Walter et al., 2015). Experiments were held at temperature for up to one hour between ∼35 and 89 GPa and ∼1600 and 2200 K, as reported in Table S1. The temperature was taken as a temporal average of the maximum recorded temperature at each time step, while the error in temperature was determined from the standard deviation from this mean value. The temporal and spatial average of the temperature recorded over the 1-D profile at each time step is also provided in Table S1.

Pressure was determined before and after heating from the Raman shift of the singlet peak of the diamond anvil at the culet surface that is related to stress in the (001) direction (Hanfland et al., 1986). We use confocal micro-Raman spectroscopy as described below and the Raman shift is calibrated for pressure relative to the ruby scale (Mao et al., 1986) using the calibration of Walter et al. (2015). The measurement precision is about 0.1 GPa and the accuracy ∼2 GPa due to uncertainty in measuring the ruby pressure in the calibration. Pressures are reported as post-heating measurements and are typically within 5% of the pre-heating pressure. No correction is made for thermal pressure during heating, which may be of the order 10% or less of the post-heating pressure at the modest temperatures in this study (Belonoshko and Dubrovinsky, 1997; Heinz, 1990).

2.3. Synchrotron X-ray diffraction

Angle-dispersive X-ray diffraction (XRD) measurements were collected from pressure–temperature quenched samples recovered from the DAC, or temperature-quenched samples at high pressure, at beamline I15 at the Diamond Light Source, UK, with an X-ray wavelength $\lambda = 0.4246$ Å. A 20 μm incident beam pinhole collimator was employed and two-dimensional diffraction patterns were measured using a MAR charge-coupled device (CCD) detector. Diffraction was taken whenever possible at the centre of the heated spot(s) as recorded during the experiment. For samples FMSC1-26 to 32 and CMSC3-21, P–T quenched XRD measurements were collected using a MAR CCD detector at beamline ID27 at the European Synchrotron Radiation Facility (ESRF), France, with a micro-focused X-ray beam with dimensions of 3×4 μm^2 and wavelength $\lambda = 0.37388$ Å. The sample to detector distance was calibrated using the diffraction patterns measured for CeO_2 or LaB_6

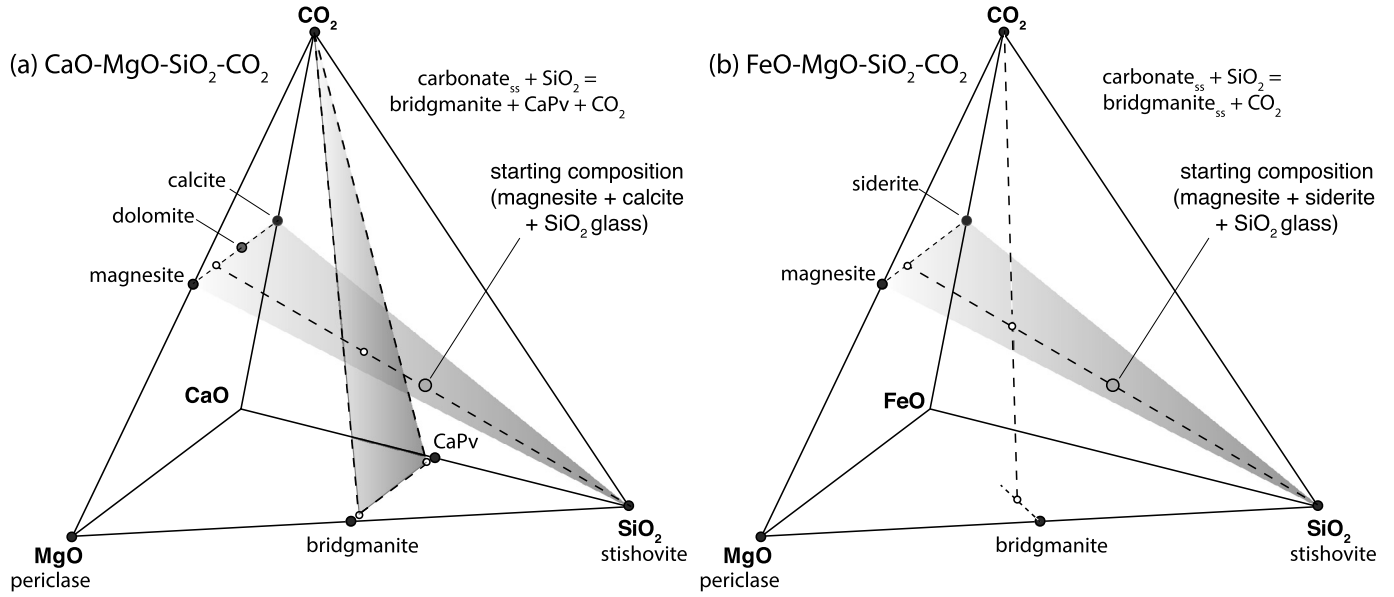

Fig. 2. Quaternary diagrams in the systems (a) CaO–MgO–SiO_2–CO_2 and (b) FeO–MgO–SiO_2–CO_2 illustrating our approach to choosing starting compositions and detecting decarbonation reactions. Starting mixtures are confined to ternary planes defined by carbonate + SiO_2, and decarbonation produces quaternary phases such as bridgmanite, Ca-perovskite (CaPv) and CO_2, or quinary phases if C (diamond) + O_2 are reaction products.

standards and integrated to one-dimensional profiles, accounting for geometrical effects and incident beam polarisation, using the program GSAS-II (Toby and Von Dreele, 2013). Lattice parameters of quenched phase were determined by full profile fitting of the diffraction profiles using the Le Bail method (Le Bail et al., 1988) as implemented in the GSAS suite of programmes (Larson and Von Dreele, 1994; Toby, 2001).

2.4. Micro-Raman spectroscopy

Micro-Raman spectroscopy was utilised for pressure measurement and to identify the presence of diamond and CO_2 in run products. Spectra were acquired with a Jobin-Yvon T64000 triple spectrometer operating in confocal mode with 2400 gr/mm gratings. Typical spectral resolution is ~0.1–0.3 cm^{-1} depending on spectrometer configuration. A 532 nm laser is focused onto the sample through a 50x long working distance objective creating a ~3 to 5 μm spot on the sample. When measuring sample pressure in the DAC, the laser is focused at the culet surface, and the confocal resolution is maximized. After heating, pressure is measured in the same place the sample was heated. When searching for diamond in *P–T* quenched run products, a Raman map covering the sample chamber was made using a grid of points with 3–5 μm steps, and 10–30s acquisitions at each point with spectra centered on the 1332 cm^{-1} diamond vibration. When searching for CO_2 in *T*-quenched run products confocal Raman spectra are taken from 200 to 1300 cm^{-1} with acquisition times of up to four hours.

3. Results

3.1. Evidence for decarbonation reactions

Experimental conditions and the phases identified by XRD and Raman in the quenched run products are provided in Table S1. In addition to the synthesized silicate and carbon-bearing phases, diffraction patterns also contain peaks from the Re gasket, Pt-black absorber, and NaCl pressure media. The experiments reported on here are synthesis experiments and phase boundaries have not been reversed. Most experiments were made at a single pressure and temperature with the aim of detecting whether a decarbonation reaction occurred by interrogating quenched samples for the presence of non-ternary phases (i.e. bridgmanite, Ca-perovskite, diamond or CO_2).

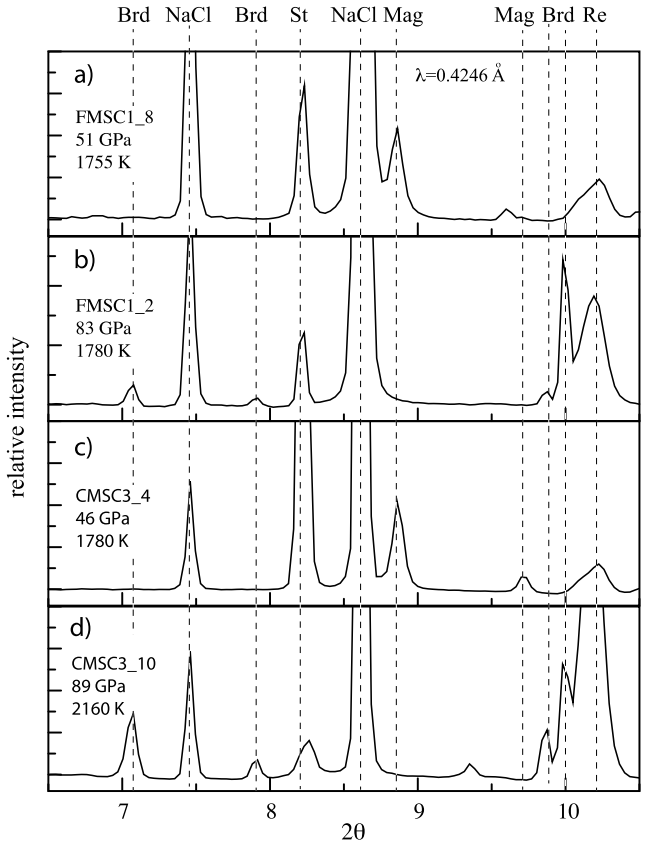

Fig. 3. Selected X-ray diffraction patterns showing relative intensity versus scattering angle 2θ for *P–T* quenched run products in the CMSC and FMSC systems (see Table S1). The diffraction lines are labelled according to identified phases; Brd = bridgmanite, St = stishovite, Mag = magnesite as well as the NaCl pressure medium and Re gasket.

3.1.1. Identification of non-ternary silicate phases by X-ray diffraction

Fig. 3 shows diffraction patterns from the FMSC and CMSC systems that illustrate the detection of decarbonation reactions in our synthesis experiments. In experiments P–T quenched from 51 GPa and 1755 K (FMSC) and 46 GPa and 1780 K (CMSC) we observe the presence of stishovite and carbonate in the run products with no indication of a reaction to form bridgmanite (Fig. 3a and 3c). In contrast, in experiments at higher pressures (Fig. 3b and 3d) the synthesized run products contain bridgmanite with all of the carbonate phase exhausted. These diffraction patterns are typical of those obtained from run products and illustrate the unequivocal occurrence of decarbonation reactions by identifying the presence of non-ternary bridgmanite. However, the nature of the carbon-bearing phase produced upon decarbonation is not always obvious from diffraction alone.

3.1.2. Detection of diamond phases by Raman

The products of the decarbonation reactions that produce bridgmanite and/or Ca-perovskite must also produce CO_2, or $C + O_2$, in reactions analogous to (1)–(5) above. Both C (diamond) and CO_2 (phase V) are challenging to detect with X-ray diffraction due to their low scattering efficiency and given the tiny volume of material being probed in our experiments ($\sim$2000 μm^3 for diffraction and 50 μm^3 for Raman). To aid in the detection of diamond, each P–T quenched run product was mapped with a confocal Raman microscope as described above. We found that diamond is readily detected with this method and diamond-bearing experiments typically show a well-defined 1332 cm^{-1} fundamental Raman vibration. Fig. 4 shows examples typical of X-ray and Raman detection of diamond in P–T quenched experiments in the CMSC system. Here we rely on a combination of Raman mapping and X-ray diffraction for detecting diamond in experiments with Raman providing the most definitive observations (Table S1).

At the P–T conditions of the experiments reported here, if present CO_2 should be in the form of solid phase V (Iota et al., 2007). In P–T quenched samples any solid CO_2 formed by reaction will outgas upon decompression. Therefore, we searched for evidence of solid CO_2–V by *in situ* diffraction in a temperature-quenched experiment at 65 GPa (CMSC3_16) but were unable to identify any diffraction lines. To further test for the presence of CO_2–V we made two experiments without a pressure medium to maximize the amount of material present (CMSC3_18 and CMSC3_19, Table S1). The temperature-quenched run products were examined using confocal Raman and the results are shown in Supplemental Figure S1. We view these results as inconclusive but note that the Raman patterns taken at 63 and 75 GPa, although weak, are suggestive of the presence of solid CO_2–V in the run products. Our ability to define reaction boundaries does not depend on detection of CO_2 and we assume the presence of solid CO_2–V in experiments where we observe the formation of bridgmanite but do not observe the presence of diamond.

3.1.3. Detection of Ca-perovskite in the CMSC system

Fig. 2a shows that the presence of bridgmanite requires a non-ternary reaction that produces CO_2 (or $C + O_2$), and because of the relatively small Ca substitution into bridgmanite another calcic phase is required for mass balance in the CMSC system (e.g. reaction (5)). Ca-perovskite is the likely candidate, but this phase becomes amorphous on pressure quenching and was not clearly detectable in our P–T quenched samples by diffraction. To confirm the presence of Ca-perovskite and to investigate the nature of the carbonate phase at high pressure, we made high-P *in situ* measurements in experiment CMSC3_16. In this experiment we first heated to 1738 K at 55 GPa for 20 minutes and did not detect the presence of either bridgmanite or Ca-perovskite. We then increased pressure to 65 GPa and heated at 1780 K for 30 minutes.

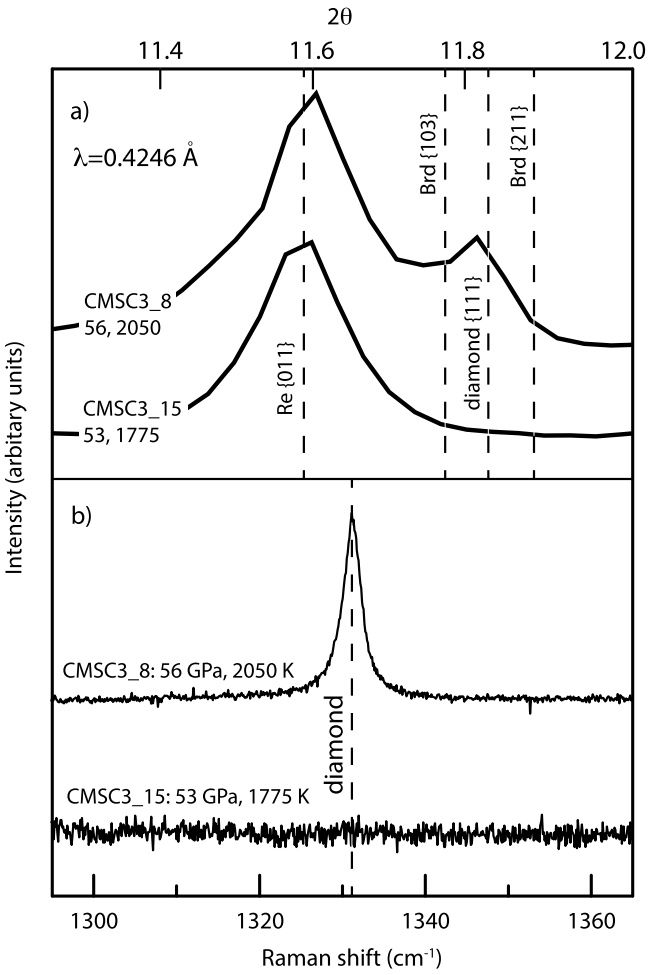

Fig. 4. Example X-ray diffraction patterns (a) and Raman spectra (b) illustrating the detection of diamond in P–T quenched run products in the CMSC system. Dashed lines in (a) show diffraction lines for Re gasket, bridgmanite and diamond and in (b) show the position of the fundamental Raman peak for diamond. Note that CMSC3_15 shows no indication of diamond in either diffraction or Raman spectra, whereas experiment CMSC3_8 shows the presence of diamond in both.

Fig. 5 is the diffraction pattern taken at 65 GPa that shows the coexistence of bridgmanite and Ca-perovskite together with SiO_2 in the $CaCl_2$ structure, as required by chemography (Fig. 2); note that at pressures above $\sim$60 GPa the expectation is that the $CaCl_2$ phase is the stable SiO_2 polymorph in all our experiments. From these observations, we assume that all experiments in the CMSC system in which bridgmanite forms by decarbonation also contain Ca-perovskite.

3.2. Carbonate phases

Our P–T quenched experiments in the FMSC and CMSC systems show the presence of a magnesite-structured phase in carbonate-bearing run products. In the FMSC system, chemography dictates a ferro-magnesite solid solution at the experimental conditions (Fig. 2b), and diffraction taken at high pressure in this system (Table S1) confirms a magnesite-structured phase.

In the CMSC system, on the basis of the 3:1 molar mixture of $MgCO_3$:$CaCO_3$ in the starting composition, we expect either a complete solid solution or a two-phase mixture (e.g. magnesite plus a dolomite stoichiometry phase or magnesite plus a $CaCO_3$ phase) at experimental conditions (Fig. 2a). Diffraction patterns from P–T quenched run products are dominated by magnesite, but all but one of the magnesite-bearing experiments contain a diffuse, low

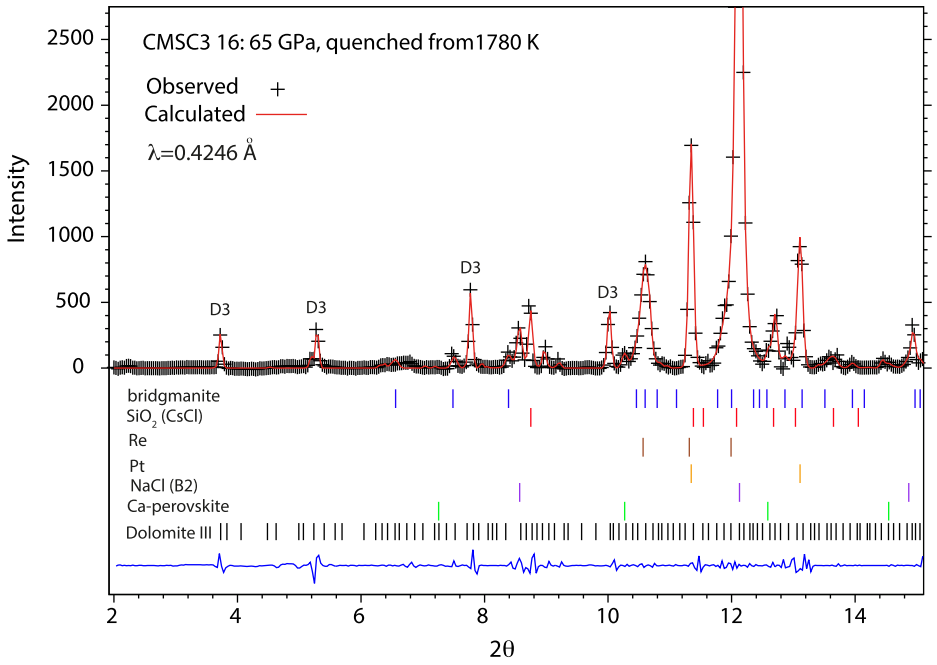

Fig. 5. Full profile GSAS fit to a diffraction pattern in sample CMSC3_16 taken at 65 GPa and quenched from 1780 K. The diffraction pattern shows the presence of a carbonate phase with multiple peaks that index to a dolomite III structured phase (Merlini et al., 2012). The pattern also shows the presence of bridgmanite and Ca-perovskite, which are products of a decarbonation reaction between carbonate and stishovite (also present).

to medium intensity peak that can be indexed to the most intense calcite line (104), although we could not identify any other calcite lines. In contrast, there is no indication of magnesite or a $CaCO_3$ phase in diffraction patterns taken at 65 GPa in experiment CMSC3_16 which contains Brd + Ca–Pv + St as described above, but a decent full profile fit to the pattern is obtained (e.g. Fig. 5) when starting with the unit cell parameters for dolomite III as reported in an experiment at 56 GPa by Merlini et al. (2012) and making minor adjustments to account for pressure. As the phase is triclinic there are many diffraction lines, but the low angle peaks of a dolomite III structured phase are especially diagnostic in the diffraction pattern (Fig. 5). This result suggests that in the CMSC system a solid solution exists between $CaMg(CO_3)_2$ and $MgCO_3$ at lower mantle conditions with a dolomite III like structure, yielding the decarbonation reaction where x is mole fraction from 0 to 1:

$$Ca_xMg_{(2-x)}(CO_3)_2 + 2SiO_2 = (2-x)MgSiO_3 + xCaSiO_3 + 2CO_2 \quad (6)$$

Luth (2001) showed that in the CaO–MgO–CO_2 system $CaMg(CO_3)_2$ dolomite is unstable relative to magnesite + calcite at pressure above ~10 GPa at ~1600 K with the reaction boundary having a positive Clapyron slope. Biellmann et al. (1993) observed magnesite and calcite in *P–T* quenched run products in LH-DAC experiments at 20 and 50 GPa (1500–2500 K) using a bulk composition comprising $CaMg(CO_3)_2$ and natural enstatite in apparent contradiction to our observations of a stable dolomite III structured phases at high pressure. However, we observe that dolomite structured phases are not present in our *P–T* quenched run products and we observe magnesite ± calcite, suggesting that the dolomite III structured phase is unquenchable and the presence of magnesite ± minor calcite indicates un-mixing of the carbonate upon pressure quenching. This unmixing also explains the results of Biellmann et al. (1993), as they made observations based only on *P–T* quenched run products. Merlini et al. (2012, 2017) suggested that the presence of minor amounts of iron stabilize the high-pressure dolomite phases relative to magnesite + calcite at high pressure. Our results indicate that dolomite III structured phases could be stable relative to magnesite + $CaCO_3$ phases in the lower mantle even in the iron-free system, although further investigations are needed to verify the stable carbonate phase in subducted oceanic crust.

3.3. Decarbonation phase relations

Experimental results in the FMSC and CMSC systems are plotted on *P–T* diagrams in Fig. 6. On the basis of our synthesis experiments we define three general reactions common to both systems. Decarbonation reaction (a) is the breakdown of carbonate in the presence of SiO_2 to form bridgmanite ± Ca-perovskite (CMSC) + CO_2 (e.g. reactions (4) and (5) above). The position of this reaction boundary is best bracketed in the FMSC system and is constrained to have a negative Clapeyron slope (Fig. 6a). In this system reaction (a) is divariant as both ferromagnesite and bridgmanite are solid solutions, and so it occurs over a *P–T* range rather than along a single univariant boundary. On the basis of experiments where magnesite is eliminated in the reaction, the indication is that for our bulk composition the width of the boundary is < 10 GPa, as shown schematically on Fig. 6a. In the CMSC system decarbonation reaction (a) is nearly coincident but possibly at a somewhat higher pressure than the reaction in the FMSC system.

Reaction (b) in Fig. 6 is a decarbonation reaction in which C (diamond) + O_2 is produced directly from reaction of carbonate with SiO_2. While our data do not constrain the position of this reaction it must occur as a result of intersection of the breakdown reaction (c) $CO_2 = C + O_2$ with decarbonation reaction (a). The experiments containing diamond indicate a slightly negative slope to reaction (c) in the FMSC system, and we have drawn a similar reaction boundary in the CMSC system although the slope is not well constrained. Data from the two systems are consistent in indicating that above ~1800 to 1900 K, CO_2 breaks down to diamond plus O_2 over the entire pressure range investigated. In the region between reactions (a) and (c) on Fig. 6 the stable carbon-bearing phase is CO_2–V.

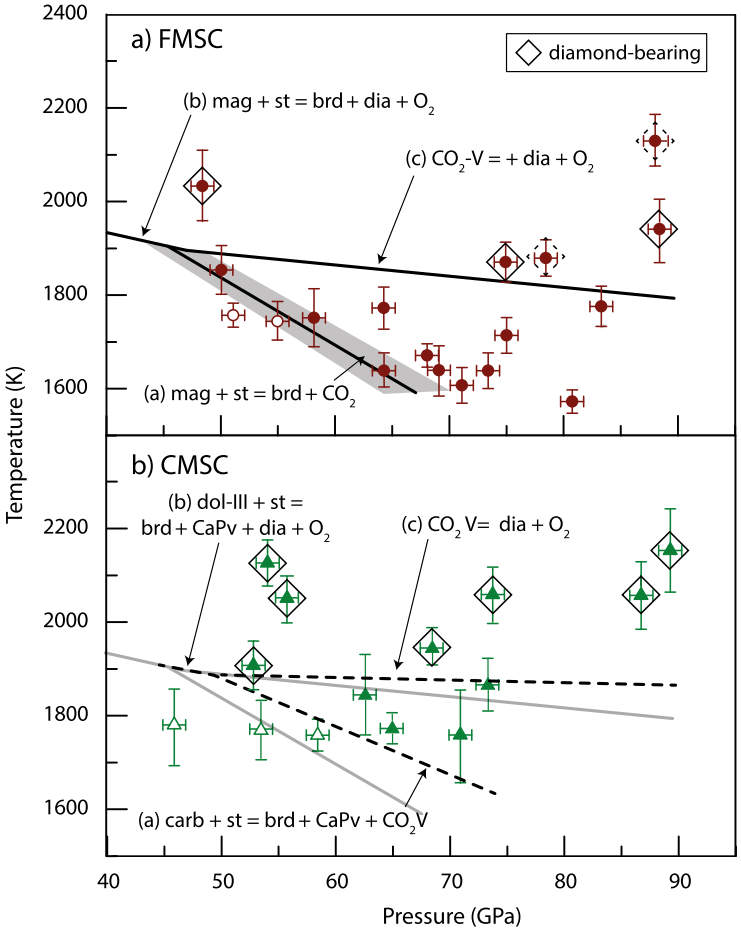

Fig. 6. Pressure–temperature plots showing decarbonation reaction boundaries in a) the FMSC and b) the CMSC systems. In panel b) the dashed lines are reaction boundaries in the CMSC system and the grey lines are from the FMSC system for comparison. Open symbols indicate experiments where carbonate and silica are stable and filled symbols indicate experiments where the presence of non-ternary phases formed in decarbonation reactions, which are labelled. Symbols encased in a diamond indicate the presence of diamond in run products, and broken diamonds denote samples where the presence of diamond remains ambiguous.

Previous experiments show that at pressures up to 25 GPa decarbonation occurs upon melting in the MSC system, with a melting temperature at 25 GPa of ~2100 K (Kakizawa et al., 2015), already hundreds of degrees above the temperatures of the decarbonation reactions observed at 40 GPa and above in this study. A possible explanation for the change from a melting decarbonation reaction at lower pressures to a subsolidus decarbonation reaction at higher pressures as observed in this and other studies is the negative slopes of the decarbonation reactions (Fig. 6). At lower pressures the decarbonation reaction occurs at higher temperatures, and when the decarbonation reaction intersects the melting curve in a carbonate-silicate system, melting of the carbonate component occurs at a lower temperature than does solid state decarbonation.

Melting temperatures in the FMSC and CMSC systems have not been determined at lower mantle pressures. We note that all the temperatures reported on here are lower than the melting curves in the $MgSiO_3$–$MgCO_3$ and $MgCO_3$–$CaCO_3$ systems as determined in our lab (Thomson et al., 2014), with the key experiments that bracket the decarbonation reaction hundreds of degrees lower than this melting determination. We did not observe any thermal perturbations indicative of melting during temperature ramping (Lord et al., 2014a; Lord et al., 2014b; Walter et al., 2015) or during the long, nearly isothermal heating periods. We do note that in several failed experiments, samples 'flashed' during heating to some unknown but much higher temperature. These samples may have melted, but in any case, we deem them unreliable in terms of constraining phase relations and in each case diamond was formed in the experiment.

Fig. 7 shows reaction boundaries from the FMSC system compared to reactions observed in previous studies in the MSC and CSC systems as shown in Fig. 1 (Li et al., 2018; Maeda et al., 2017; Seto et al., 2008; Zhang et al., 2018). The negative Clapeyron slope of the decarbonation reaction in FMSC (e.g. Mgs + St = Brd + CO_2) is consistent with that found for this reaction in the MSC system (Maeda et al., 2017), however, we locate it ~400–500 K lower in temperature. We note that the decarbonation reaction in FMSC is nearly coincident with the CO_2 = C + O_2 reaction boundary found by Litasov et al. (2011) on samples of pure CO_2. In contrast to decarbonation reactions found in this study and in the MSC system, the decarbonation reaction boundary in the CMC system has a positive Clapyron slope on the basis of both experiment and theory (Li et al., 2018; Zhang et al., 2018).

A significant difference between our study and that of Maeda et al. (2017) in the MSC system is the location of the CO_2 breakdown reaction to form diamond plus oxygen (Fig. 7). These authors label the reaction as bridgmanite + CO_2 =bridgmanite + C + O_2. However, unless bridgmanite participates in the reaction (e.g. solution of silicate and CO_2), this is effectively the CO_2 breakdown reaction, CO_2 =C + O_2. Maeda et al. (2017) locate a steep, temperature insensitive reaction at ~80 GPa that is inconsistent with the much shallower negative slope of the CO_2 breakdown reaction found by Litasov et al. (2011) and the decarbonation reactions found in this study. Our diamond-forming CO_2 breakdown reaction has a less shallow slope than that of Litasov et al. overlapping in

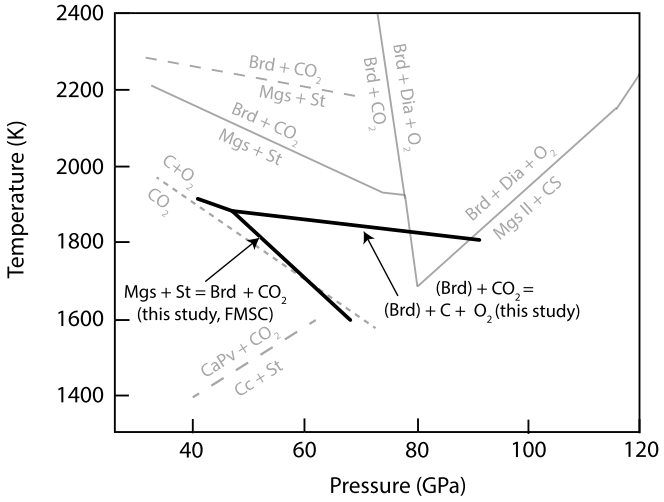

Fig. 7. Pressure–temperature diagram showing decarbonation reactions observed in this study in the FMSC system relative to decarbonation reactions observed in the MSC, CSC and C-O systems with reaction boundaries and phase labels as in Fig. 1.

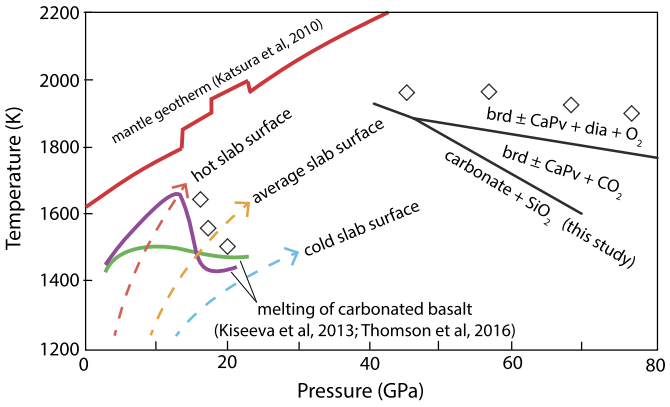

Fig. 8. Pressure–temperature diagram showing generalised carbonate phase relations in subducted, carbonated oceanic crust. The melting curves of carbonated basalt at upper mantle and transition zone pressures are from Kiseeva et al. (2013) (green curve) and Thomson et al. (2016a, 2016b) (purple curve). Also shown are model geotherms at the surface of subducted oceanic crust and a mantle geotherm (Katsura et al., 2010; Syracuse et al., 2010). Diamond symbols show schematically where diamond can be produced via subduction of carbonated oceanic crust. (For interpretation of the colors in the figure(s), the reader is referred to the web version of this article.)

temperature at ~40 GPa. The difference between the CO_2 breakdown reaction in our study and that in Litasov et al. could result from solution of bridgmanite into CO_2 or vice versa although we have no evidence to confirm or refute this possibility.

4. The fate of deeply subducted carbonate in oceanic crust

Fig. 8 shows generalised phase relations for carbonated oceanic crust that survives beyond the volcanic front at subduction zones. Deeply subducted carbonate in oceanic crust may induce melting of oceanic crust in the transition zone along all but the coolest slab-surface geotherms due to a pronounced reduction in the solidus of carbonated basalt at these depths (Kiseeva et al., 2013; Thomson et al., 2016b). Indeed, mineral inclusions in sublithospheric diamonds from the deep upper mantle and transition zone testify to a role for carbonated melt from oceanic crust in their origin (Bulanova et al., 2010; Thomson et al., 2016a; Walter et al., 2008), and also carry considerable evidence for recycled oceanic crustal materials both in the carbon isotopic composition of the diamonds and the oxygen isotopic composition of the inclusions (Burnham et al., 2015; Ickert et al., 2013). Thus, carbon may be added to the deep upper mantle and transition zone in the form of diamond by melting of carbonated of oceanic crust and reaction of carbonated melts with reducing mantle (Rohrbach and Schmidt, 2011; Walter et al., 2008). As the presence of diamond does not lower the melting point of mantle peridotite, carbon added as diamond can be potentially stored in the transition zone, although mantle circulation may recycle this carbon back to the surface at oceanic spreading centers as it is captured in mantle upwelling beneath mid-oceanic ridges, oxidized to carbonate and melted ('redox melting') (Dasgupta and Hirschmann, 2010; Stagno et al., 2013). If oceanic crustal carbonate can avoid melting in the transition zone along cooler geotherms, or perhaps due to a higher solidus in more calcic compositions (e.g. Kiseeva et al., 2013) (Fig. 8), then some fraction of carbonate may be subducted into the lower mantle in oceanic crust.

Seismic tomography indicates that most subducting lithospheric slabs eventually sink to the base of the mantle (Van der Voo et al., 1999; Van der Hilst et al., 1997), where they accumulate at the core mantle boundary and presumably reside over long timescales. Our results show that reaction of carbonate with silica at ~40 to 60 GPa creates a final barrier to subduction of carbonate in oceanic crust into the deeper lower mantle (Fig. 8). Indeed, decarbonation reactions effectively preclude transport of carbonate in oceanic crust to depths greater than ~1500 km. Our results indicate that CO_2–V may be stable in oceanic crust over some mid-lower mantle depth range that would depend on the geotherm, but we predict that CO_2 dissociation will make diamond the stable form of carbon in oceanic crust subducted into the deepest lower mantle. Diamond will be stable in oceanic crust that stagnates in the lower mantle and thermalizes with the mantle geotherm throughout the lower mantle (Fig. 8).

Carbon in subducted oceanic crust at the base of the mantle should remain stable because diamond is refractory and immobile and will not lower the melting point of the silicate. Diamond is therefore a potential host for long-term deep mantle storage of carbon and could potentially contribute to the low H/C ratio of the mantle relative to the exosphere (Hirschmann and Dasgupta, 2009). On the basis of a modern annual subduction flux of C (as CO_2 in carbonate) in subducted oceanic crust of ~25 Mt/year (Kelemen and Manning, 2015) and assuming as an endmember case that the entire budget of carbonate in oceanic crust survives to the lower mantle and dissociates to C + O_2, for an arbitrary primordial lower mantle carbon content of 100 ppm the carbon content of the lower mantle would increase by ~8% in 3 Ga, or by as much as ~80% for a primordial C content of 10 ppm. Thus, as pointed out by Hirschmann and Dasgupta (2009) for subduction and deep retention of carbon to be a viable mechanism to account for the mantle H/C ratio, subducting slabs would need to dehydrate and return hydrogen to the surface while retaining carbon, and the majority of mantle carbon would be recycled.

Release of oxygen as a product of carbonate or CO_2 dissociation could be a source of net lower mantle oxidation. Using the same model assumptions as for carbon, and assuming that all the oxygen was mobilized and incorporated into the lower mantle, the oxygen content of the lower mantle as a whole would increase by only ~0.01% over a 3 Ga timeframe. However, the release of oxygen by decarbonation would likely locally oxidize silicates (e.g. bridgmanite) in oceanic crust rather than oxidizing ambient mantle, so that there would be no net oxidation of the slab by this mechanism. We reiterate that considerable carbonate loss from subducted oceanic crust is expected for most subduction geotherms either through dissolution in fluids in the upper mantle or melting of carbonated oceanic crust at transition zone depths, and the potential flux of carbon and oxygen into the lowermost mantle in subducted

oceanic crust may be much less than in these endmember estimates.

Evidence for deep subduction of carbon potentially comes from ocean-island basalts (OIB) which have distinctly elevated carbon contents ($>$ 1000 ppm) relative to depleted MORB ($<$ 100 ppm) (Dasgupta and Hirschmann, 2010). The OIB source has long been considered to have a recycled oceanic crustal component based on its distinct geochemistry (Hawkesworth et al., 1979; Hofmann, 1997), and oceanic crust subducted into the deepest lower mantle may be an important component in plumes that originate from near the core-mantle boundary. Thus, elevated carbon in OIB may potentially be attributed to subducted carbon stored as diamond in oceanic crust in the deepest lower mantle. Only upon upwelling to the shallower mantle along a hot mantle geotherm would diamond be expected to eventually oxidize to carbonate, lowering the solidus of the silicate and contributing to melting in the transition zone or upper mantle and becoming incorporated into OIB melts.

5. Conclusions

We made laser-heated diamond anvil cell experiments in the FMSC and CMSC systems to investigate the stability of carbonate in oceanic crust subducted into the lower mantle. Our results show that carbonate will react with silica at pressures of ~40 to 70 GPa in a decarbonation reaction of the form: carbonate + silica = bridgmanite ± Ca-perovskite + CO_2–V. This reaction has a negative Clapeyron slope and presents a final barrier to subduction of carbonate beyond mid-lower mantle depths. Solid CO_2–V can remain stable over some depth range in subducted oceanic crust but will eventually breakdown to diamond and oxygen at mantle temperatures. Thus, the fate of carbonate deposited in oceanic crust at the surface is ultimately diamond at conditions of the deep lower mantle where it may be stored on long timescales and returned to the surface in upwelling plumes.

Acknowledgements

Financial support for this study was provided by NERC grant NE/M000419/1 to M.J. Walter. O.T. Lord would like to acknowledge support from the Royal Society in the form of a University Research Fellowship (UF150057) and from the NERC in the form of a post-doctoral research fellowship (NE/J018945/1). We acknowledge the ESRF for provision of beam time under proposal ES736 and G. Garborino for their assistance at beamline ID27. We thank A. Thomson, C. Gregson, M. Baron, and D. Daisenberger, for their assistance during synchrotron beamtime at the DLS. Measurements at DLS were made under beamtime awards EE10617, EE11896, EE15288, and EE17994. Data are available at the University of Bristol data repository, data.bris, at https://doi.org/10.5523/bris.75f6kxwjf3m02cc74duvve592.

Appendix A. Supplementary material

Supplementary material related to this article can be found online at https://doi.org/10.1016/j.epsl.2019.01.041.

References

Bayarjargal, L., Fruhner, C.J., Schrodt, N., Winkler, B., 2018. $CaCO_3$ phase diagram studied with Raman spectroscopy at pressures up to 50 GPa and high temperatures and DFT modeling. Phys. Earth Planet. Inter. 281, 31–45.

Belonoshko, A.B., Dubrovinsky, L.S., 1997. A simulation study of induced failure and recrystallization of a perfect MgO crystal under non-hydrostatic compression: application to melting in the diamond-anvil cell. Am. Mineral. 82, 441–451.

Biellmann, C., Gillet, P., Guyot, F., Peyronneau, J., Reynard, B., 1993. Experimental-evidence for carbonate stability in the earths lower mantle. Earth Planet. Sci. Lett. 118, 31–41.

Brenker, F.E., Vollmer, C., Vincze, L., Vekemans, B., Szymanski, A., Janssens, K., Szaloki, I., Nasdala, L., Joswig, W., Kaminsky, F., 2007. Carbonates from the lower part of transition zone or even the lower mantle. Earth Planet. Sci. Lett. 260, 1–9.

Bulanova, G.P., Walter, M.J., Smith, C.B., Kohn, S.C., Armstrong, L.S., Blundy, J., Gobbo, L., 2010. Mineral inclusions in sublithospheric diamonds from Collier 4 kimberlite pipe, Juina, Brazil: subducted protoliths, carbonated melts and primary kimberlite magmatism. Contrib. Mineral. Petrol. 160, 489–510.

Buob, A., Luth, R.W., Schmidt, M.W., Ulmer, P., 2006. Experiments on $CaCO_3$–$MgCO_3$ solid solutions at high pressure and temperature. Am. Mineral. 91, 435–440.

Burnham, A.D., Thomson, A.R., Bulanova, G.P., Kohn, S.C., Smith, C.B., Walter, M.J., 2015. Stable isotope evidence for crustal recycling as recorded by superdeep diamonds. Earth Planet. Sci. Lett. 432, 374–380.

Chen, B., Li, Z.Y., Zhang, D.Z., Liu, J.C., Hu, M.Y., Zhao, J.Y., Bi, W.L., Alp, E.E., Xiao, Y.M., Chow, P., Li, J., 2014. Hidden carbon in Earth's inner core revealed by shear softening in dense Fe_7C_3. Proc. Natl. Acad. Sci. USA 111, 17755–17758.

Coogan, L.A., Dosso, S.E., 2015. Alteration of ocean crust provides a strong temperature dependent feedback on the geological carbon cycle and is a primary driver of the Sr-isotopic composition of seawater. Earth Planet. Sci. Lett. 415, 38–46.

Coogan, L.A., Gillis, K.M., 2013. Evidence that low-temperature oceanic hydrothermal systems play an important role in the silicate-carbonate weathering cycle and long-term climate regulation. Geochem. Geophys. Geosyst. 14, 1771–1786.

Dasgupta, R., Hirschmann, M.M., 2010. The deep carbon cycle and melting in Earth's interior. Earth Planet. Sci. Lett. 298, 1–13.

Dasgupta, R., Walker, D., 2008. Carbon solubility in core melts in a shallow magma ocean environment and distribution of carbon between the Earth's core and the mantle. Geochim. Cosmochim. Acta 72, 4627–4641.

Frost, D.J., McCammon, C.A., 2008. The redox state of Earth's mantle. Annu. Rev. Earth Planet. Sci. 36, 389–420.

Gavryushkin, P.N., Martirosyan, N.S., Inerbaev, T.M., Popov, Z.I., Rashchenko, S.V., Likhacheva, A.Y., Lobanov, S.S., Goncharov, A.F., Prakapenka, V.B., Litasov, K.D., 2017. Aragonite-II and $CaCO_3$-VII: new high-pressure, high-temperature polymorphs of $CaCO_3$. Cryst. Growth Des. 17, 6291–6296.

Gorman, P.J., Kerrick, D.M., Connolly, J.A.D., 2006. Modeling open system metamorphic decarbonation of subducting slabs. Geochem. Geophys. Geosyst. 7.

Halliday, A.N., 2013. The origins of volatiles in the terrestrial planets. Geochim. Cosmochim. Acta 105, 146–171.

Hanfland, M., Syassen, K., Fahy, S., Louie, S.G., Cohen, M.L., 1986. The 1st-order Raman mode of diamond under pressure. Physica B & C 139, 516–519.

Hawkesworth, C.J., Norry, M.J., Roddick, J.C., Vollmer, R., 1979. Nd-143-Nd-144 and Sr-87-Sr-86 ratios from the Azores and their significance in LIL-element enriched mantle. Nature 280, 28–31.

Heinz, D.L., 1990. Thermal pressure in the laser-heated diamond anvil cell. Geophys. Res. Lett. 17, 1161–1164.

Hirschmann, M.M., Dasgupta, R., 2009. The H/C ratios of Earth's near-surface and deep reservoirs, and consequences for deep Earth volatile cycles. Chem. Geol. 262, 4–16.

Hofmann, A.W., 1997. Mantle geochemistry: the message from oceanic volcanism. Nature 385, 219–229.

Ickert, R.B., Stachel, T., Stern, R.A., Harris, J.W., 2013. Diamond from recycled crustal carbon documented by coupled delta O-18-delta C-13 measurements of diamonds and their inclusions. Earth Planet. Sci. Lett. 364, 85–97.

Iota, V., Yoo, C.S., Klepeis, J.H., Jenei, Z., Evans, W., Cynn, H., 2007. Six-fold coordinated carbon dioxide VI. Nat. Mater. 6, 34–38.

Isshiki, M., Irifune, T., Hirose, K., Ono, S., Ohishi, Y., Watanuki, T., Nishibori, E., Takata, M., Sakata, M., 2004. Stability of magnesite and its high-pressure form in the lowermost mantle. Nature 427, 60–63.

Kakizawa, S., Inoue, T., Suenami, H., Kikegawa, T., 2015. Decarbonation and melting in $MgCO_3$–SiO_2 system at high temperature and high pressure. J. Mineral. Petrol. Sci. 110, 179–188.

Katsura, T., Yoneda, A., Yamazaki, D., Yoshino, T., Ito, E., 2010. Adiabatic temperature profile in the mantle. Phys. Earth Planet. Inter. 183, 212–218.

Kelemen, P.B., Manning, C.E., 2015. Reevaluating carbon fluxes in subduction zones, what goes down, mostly comes up. Proc. Natl. Acad. Sci. USA 112, E3997–E4006.

Kerrick, D.M., Connolly, J.A.D., 2001. Metamorphic devolatilization of subducted oceanic metabasalts: implications for seismicity, arc magmatism and volatile recycling. Earth Planet. Sci. Lett. 189, 19–29.

Kiseeva, E.S., Litasov, K.D., Yaxley, G.M., Ohtani, E., Kamenetsky, V.S., 2013. Melting and phase relations of carbonated eclogite at 9–21 GPa and the petrogenesis of alkali-rich melts in the deep mantle. J. Petrol. 54, 1555–1583.

Larson, A.C., Von Dreele, R.B., 1994. General Structure Analysis System (GSAS). Los Alamos National Laboratory Report LAUR, pp. 86–748.

Le Bail, A., Duroy, H., Fourquet, J.L., 1988. Ab initio structure determination of lisbwo6 by X-ray-powder diffraction. Mater. Res. Bull. 23, 447–452.

Li, X.Y., Zhang, Z.G., Lin, J.F., Ni, H.W., Prakapenka, V.B., Mao, Z., 2018. New high-pressure phase of $CaCO_3$ at the topmost lower mantle: implication for the deep-mantle carbon transportation. Geophys. Res. Lett. 45, 1355–1360.

Litasov, K.D., Goncharov, A.F., Hemley, R.J., 2011. Crossover from melting to dissociation of CO_2 under pressure: implications for the lower mantle. Earth Planet. Sci. Lett. 309, 318–323.

Lobanov, S.S., Dong, X., Martirosyan, N.S., Samtsevich, A.I., Stevanovic, V., Gavryushkin, P.N., Litasov, K.D., Greenberg, E., Prakapenka, V.B., Oganov, A.R., Goncharov, A.F., 2017. Raman spectroscopy and X-ray diffraction of sp(3) $CaCO_3$ at lower mantle pressures. Phys. Rev. B 96.

Lord, O.T., Wann, E.T.H., Hunt, S.A., Walker, A.M., Santangeli, J., Walter, M.J., Dobson, D.P., Wood, I.G., Vocadlo, L., Morard, G., Mezouar, M., 2014a. The NiSi melting curve to 70 GPa. Phys. Earth Planet. Inter. 233, 13–23.

Lord, O.T., Wood, I.G., Dobson, D.P., Vocadlo, L., Wang, W.W., Thomson, A.R., Wann, E.T.H., Morard, G., Mezouar, M., Walter, M.J., 2014b. The melting curve of Ni to 1 Mbar. Earth Planet. Sci. Lett. 408, 226–236.

Luth, R.W., 2001. Experimental determination of the reaction aragonite plus magnesite = dolomite at 5 to 9 GPa. Contrib. Mineral. Petrol. 141, 222–232.

Maeda, F., Ohtani, E., Kamada, S., Sakamaki, T., Hirao, N., Ohishi, Y., 2017. Diamond formation in the deep lower mantle: a high-pressure reaction of $MgCO_3$ and SiO_2. Sci. Rep. 7.

Mao, H.K., Xu, J., Bell, P.M., 1986. Calibration of the ruby pressure gauge to 800-kbar under quasi-hydrostatic conditions. J. Geophys. Res. B, Solid Earth Planets 91, 4673–4676.

Mao, Z., Armentrout, M., Rainey, E., Manning, C.E., Dera, P., Prakapenka, V.B., Kavner, A., 2011. Dolomite III: a new candidate lower mantle carbonate. Geophys. Res. Lett. 38.

Marty, B., 2012. The origins and concentrations of water, carbon, nitrogen and noble gases on Earth. Earth Planet. Sci. Lett. 313, 56–66.

Merlini, M., Cerantola, V., Gatta, G.D., Gemmi, M., Hanfland, M., Kupenko, I., Lotti, P., Muller, H., Zhang, L., 2017. Dolomite-IV: candidate structure for a carbonate in the Earth's lower mantle. Am. Mineral. 102, 1763–1766.

Merlini, M., Crichton, W.A., Hanfland, M., Gemmi, M., Muller, H., Kupenko, I., Dubrovinsky, L., 2012. Structures of dolomite at ultrahigh pressure and their influence on the deep carbon cycle. Proc. Natl. Acad. Sci. USA 109, 13509–13514.

Molina, J.F., Poli, S., 2000. Carbonate stability and fluid composition in subducted oceanic crust: an experimental study on H_2O–CO_2-bearing basalts. Earth Planet. Sci. Lett. 176, 295–310.

Oganov, A.R., Ono, S., Ma, Y.M., Glass, C.W., Garcia, A., 2008. Novel high-pressure structures of $MgCO_3$, $CaCO_3$ and CO_2 and their role in Earth's lower mantle. Earth Planet. Sci. Lett. 273, 38–47.

Ono, S., Ito, E., Katsura, T., 2001. Mineralogy of subducted basaltic crust (MORB) from 25 to 37 GPa, and chemical heterogeneity of the lower mantle. Earth Planet. Sci. Lett. 190, 57–63.

Ono, S., Kikegawa, T., Ohishi, Y., 2007. High-pressure transition of $CaCO_3$. Am. Mineral. 92, 1246–1249.

Plank, T., Langmuir, C.H., 1998. The chemical composition of subducting sediment and its consequences for the crust and mantle. Chem. Geol. 145, 325–394.

Poli, S., Franzolin, E., Molina, J.F., 2009. High-pressure behaviour of carbonates and hydrates, and devolatilization of the subducted oceanic crust. Geochim. Cosmochim. Acta 73, A1038.

Ricolleau, A., Perrillat, J.P., Fiquet, G., Daniel, I., Matas, J., Addad, A., Menguy, N., Cardon, H., Mezouar, M., Guignot, N., 2010. Phase relations and equation of state of a natural MORB: implications for the density profile of subducted oceanic crust in the Earth's lower mantle. J. Geophys. Res., Solid Earth 115.

Rohrbach, A., Schmidt, M.W., 2011. Redox freezing and melting in the Earth's deep mantle resulting from carbon–iron redox coupling. Nature 472, 209–214.

Sekine, T., Irifune, T., Ringwood, A.E., Hibberson, W.O., 1986. High-pressure transformation of eclogite to garnetite in subducted oceanic-crust. Nature 319, 584–586.

Seto, Y., Hamane, D., Nagai, T., Fujino, K., 2008. Fate of carbonates within oceanic plates subducted to the lower mantle, and a possible mechanism of diamond formation. Phys. Chem. Miner. 35, 223–229.

Sleep, N.H., Zahnle, K., 2001. Carbon dioxide cycling and implications for climate on ancient Earth. J. Geophys. Res., Planets 106, 1373–1399.

Stagno, V., Frost, D.J., McCammon, C.A., Mohseni, H., Fei, Y., 2015. The oxygen fugacity at which graphite or diamond forms from carbonate-bearing melts in eclogitic rocks. Contrib. Mineral. Petrol. 169.

Stagno, V., Ojwang, D.O., McCammon, C.A., Frost, D.J., 2013. The oxidation state of the mantle and the extraction of carbon from Earth's interior. Nature 493, 84.

Syracuse, E.M., van Keken, P.E., Abers, G.A., 2010. The global range of subduction zone thermal models. Phys. Earth Planet. Inter. 183, 73–90.

Takafuji, N., Fujino, K., Nagai, T., Seto, Y., Hamane, D., 2006. Decarbonation reaction of magnesite in subducting slabs at the lower mantle. Phys. Chem. Miner. 33, 651–654.

Thomson, A.R., Kohn, S.C., Bulanova, G.P., Smith, C.B., Araujo, D., Walter, M.J., 2016a. Trace element composition of silicate inclusions in sub-lithospheric diamonds from the Juina-5 kimberlite: evidence for diamond growth from slab melts. Lithos 265, 108–124.

Thomson, A.R., Kohn, S.C., Bulanova, G.P., Smith, C.B., Araujo, D., Walter, M.J., EIMF, 2014. Origin of sub-lithospheric diamonds from the Juina-5 kimberlite (Brazil): constraints from carbon isotopes and inclusion compositions. Contrib. Mineral. Petrol. 168.

Thomson, A.R., Walter, M.J., Kohn, S.C., Brooker, R.A., 2016b. Slab melting as a barrier to deep carbon subduction. Nature 529, 76.

Toby, B.H., 2001. EXPGUI, a graphical user interface for GSAS. J. Appl. Crystallogr. 34, 210–213.

Toby, B.H., Von Dreele, R.B., 2013. GSAS-II: the genesis of a modern open-source all purpose crystallography software package. J. Appl. Crystallogr. 46, 544–549.

Van der Voo, R., Spakman, W., Bijwaard, H., 1999. Mesozoic subducted slabs under Siberia. Nature 397, 246–249.

Van der Hilst, R.D., Widiyantoro, S., Engdahl, E.R., 1997. Evidence for deep mantle circulation from global tomography. Nature 386, 578–584.

Walter, M.J., Bulanova, G.P., Armstrong, L.S., Keshav, S., Blundy, J.D., Gudfinnsson, G., Lord, O.T., Lennie, A.R., Clark, S.M., Smith, C.B., Gobbo, L., 2008. Primary carbonatite melt from deeply subducted oceanic crust. Nature 454, 622–U630.

Walter, M.J., Koga, K.T., 2004. The effects of chromatic dispersion on temperature measurement in the laser-heated diamond anvil cell. Phys. Earth Planet. Inter. 143, 541–558.

Walter, M.J., Thomson, A.R., Wang, W., Lord, O.T., Ross, J., McMahon, S.C., Baron, M.A., Melekhova, E., Kleppe, A.K., Kohn, S.C., 2015. The stability of hydrous silicates in Earth's lower mantle: experimental constraints from the systems MgO–SiO_2–H_2O and MgO–Al_2O_3–SiO_2–H_2O. Chem. Geol. 418, 16–29.

Wood, B.J., Li, J., Shahar, A., 2013. Carbon in the core: its influence on the properties of core and mantle. In: Hazen, R.M., Jones, A.P., Baross, J.A. (Eds.), Carbon in Earth, pp. 231–250.

Yaxley, G.M., Green, D.H., 1994. Experimental demonstration of refractory carbonate-bearing eclogite and siliceous melt in the subduction regime. Earth Planet. Sci. Lett. 128, 313–325.

Zhang, Z.G., Mao, Z., Liu, X., Zhang, Y.G., Brodholt, J., 2018. Stability and reactions of $CaCO_3$ polymorphs in the Earth's deep mantle. J. Geophys. Res., Solid Earth 123, 6491–6500.